



Localization Method for the Pointing Observation with the Collimated Telescopes of Insight-HXMT

Qi Luo^{1,2}, Jin-Yuan Liao¹, Yi Nang¹, Cheng-Kui Li¹, Chen Wang^{2,3}, Na Sai^{4,5}, Ju Guan¹, Yu-Peng Chen¹,
Cheng-Cheng Guo¹, Yuan Liu³, Shu Zhang¹, and Shuang-Nan Zhang^{1,2,3}

¹ Key Laboratory of Particle Astrophysics, Institute of High Energy Physics, Chinese Academy of Sciences, Beijing 100049, China; liaojiyuan@ihep.ac.cn

² University of Chinese Academy of Sciences, Beijing 100049, China

³ Key Laboratory of Space Astronomy and Technology, National Astronomical Observatories, Chinese Academy of Sciences, Beijing 100101, China

⁴ School of Physics and Technology, Wuhan University, Wuhan 430072, China

⁵ WHU-NAOC Joint Center for Astronomy, Wuhan University, Wuhan 430072, China

Received 2022 November 8; revised 2023 February 22; accepted 2023 March 15; published 2023 April 17

Abstract

An accurate target source position is sometimes useful for the pointing observation with the collimated telescopes of the Hard X-ray Modulation Telescope (Insight-HXMT), which is determined by the reliability of the instrumental response. Insight-HXMT has the unique design that all three main payloads (LE, ME and HE) consist of detector groups with three fields of views (FOVs) whose orientations differ by 60° . As the point-spread functions are different at different positions in the FOV coordinates, the count rate ratios between the detector groups depend on the position of an X-ray source in the FOVs. Based on the multi-FOV design, we develop a localization method for an X-ray source in the pointing observation of Insight-HXMT. The accuracy of the method is investigated with the pointing observations of the Crab with different exposures. We find that the statistical error decreases with the exposure, and the systematic error is dominant for the exposure >128 s. With the exposure of 1024 s, the total error is $0^\circ.015$ for the Crab. This method can effectively distinguish the Rapid Burster H 1730–333 and Slow Burster GX 354–0, which are only $0^\circ.5$ apart and can both contribute to bursts in the light curve obtained by Insight-HXMT. We also apply the pointing observation localization method to locate the X-ray counterpart of FRB 200428 with high precision. The located position is consistent with SGR J1935+2154 within 1σ uncertainty of $10'$, which provides important evidence that fast radio bursts can originate from magnetars.

Key words: instrumentation: detectors – space vehicles: instruments – telescopes

1. Introduction

The Hard X-ray Modulation Telescope (Insight-HXMT) is a slat-collimated X-ray telescope, which was launched on 2017 June (Zhang et al. 2020). There are three main payloads carried on Insight-HXMT, Low Energy X-ray Telescope (LE, 0.7–13 keV) (Chen et al. 2020), Medium Energy X-ray Telescope (ME, 5–40 keV) (Cao et al. 2020) and High Energy X-ray Telescope (HE, 20–250 keV) (Liu et al. 2020). Every telescope has three groups of FOVs whose long axis directions are placed in cross angles of 60° from one another, as shown in Figure 1. Insight-HXMT has three types of observation tasks: pointing observation for studying the spectral and temporal properties of a target source, scanning observation designed for the Galactic plane scanning survey, and gamma-ray all-sky monitoring.

X-ray imaging telescopes can obtain the positions of X-ray sources from images in their detector planes directly, e.g., focusing telescopes such as Chandra (Weisskopf et al. 2002), XMM-Newton (Jansen et al. 2001), eRosita (Predehl et al. 2010), Nustar (Harrison et al. 2013) and code-mask telescopes

such as INTEGRAL/IBIS (Ubertini et al. 2003), Swift/BAT (Barthelmy et al. 2005). X-ray collimating telescopes usually require scanning observations to determine the position of the source, such as Insight-HXMT (Sai et al. 2020). In addition, MAXI aboard the International Space Station (ISS) can perform 1D spatial modulation in the slit direction and 1D temporal modulation in the ISS scanning direction (Matsuoka et al. 2009; Hiroi et al. 2013). In the scanning observations of Insight-HXMT, the positions of X-ray sources can be inferred by the changes of the count rates with the light curve fitting method (Sai et al. 2020) and direct demodulation method (Li & Wu 1993, 1994; Guan et al. 2020). The pointing observation mode of Insight-HXMT is not originally designed for localization of sources. However, the interlaced FOVs of Insight-HXMT provide an opportunity to estimate the direction of an X-ray source in pointing observations. When a source deviates from the FOV center of Insight-HXMT, the count rates on the detectors of the three FOVs of each telescope should decrease by different amount, compared to the expected count rate if the source is in the center of the FOVs, following the shapes of the point spread functions (PSFs), thus allowing

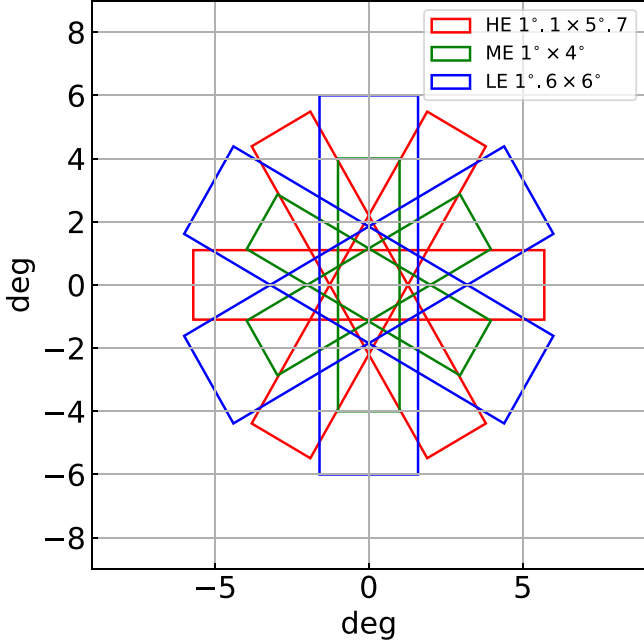


Figure 1. FOVs of the three telescopes (HE: red, ME: green, LE: blue) of Insight-HXMT.

us to obtain its position in the FOVs by fitting the count rate of each detector group with each FOV.

Fast radio bursts (FRBs) are short radio pulses observed from cosmological distances (Lorimer et al. 2007). Soft gamma-ray repeaters (SGRs) or magnetars as the sources of FRBs are predicted by some models (Petroff et al. 2019). SGR J1935+2154 was discovered by Swift in 2014 due to the occurrence of short and repeated bursts in soft gamma-rays (Stamatikos et al. 2014). It is considered a magnetar inferred from subsequent Chandra observation (Israel et al. 2014). On 2020 April 28, observations with multiple telescopes suggested that FRB 200428 originated from the magnetar SGR J1935+2154 (Bochenek et al. 2020; CHIME/FRB Collaboration et al. 2020; Margalit et al. 2020; Mereghetti et al. 2020; Li et al. 2021; Ridnaia et al. 2021; Tavani et al. 2021). The X-ray burst detected by Insight-HXMT (Li et al. 2021), INTEGRAL (Mereghetti et al. 2020), Konus-Wind (Ridnaia et al. 2021) and AGILE (Tavani et al. 2021) coincided in time with the FRB 200428 detected from the general direction of the Galactic magnetar SGR J1935+2154, and inferred a common source and the association of these events. The pointing observation localization method of HXMT provided an accurate position of the high-energy counterpart of FRB 200428 (Li et al. 2021).

This paper is organized as follows. In Section 2, we describe the principle of the method. In Section 3, we investigate the capability of the method with the pointing observations of the Crab Nebula and pulsar (hereafter the ‘‘Crab’’). The application

of the method is presented in Section 4. Finally, a summary and a discussion are given in Section 5.

2. Principle of the Localization Method

There are slat-collimators on detectors of every telescope of Insight-HXMT, which modulate the X-ray flux incident on the detectors. The count rates of Insight-HXMT can be described by:

$$C(\alpha, \beta) = C^0 \times P(\alpha, \beta) + B, \quad (1)$$

where C and B denote the count rate and background detected by a detector group, respectively; C^0 denotes the count rate of the X-ray source when the source is in the center of the FOV of the detector group. P represents the PSF which is related to the source position in the FOV. α and β are the coordinates of the source in the FOV, which can be inferred from R.A. and Dec. of the source and the attitude of the satellite. Since the sizes and directions of their FOVs are different, α and β are different for different FOVs and telescopes of Insight-HXMT. For one source with stable flux in a pointing observation, the net count rates can be described as:

$$C_{d_i}(\alpha, \beta|d_i) = C_{d_i}^0 \times P_{d_i}(\alpha, \beta|d_i), \\ i = (1, 2, 3), d = (\text{LE}, \text{ME}, \text{HE}). \quad (2)$$

The PSFs and energy response matrices of the detector groups of Insight-HXMT have already been determined from the on-ground and in-orbit calibrations (Li et al. 2020; Nang et al. 2020). We estimate the position by minimizing the χ^2 between models and data. The χ^2 can be described by:

$$\chi^2 = \sum_{i=1,2,3} \frac{(C_{L_i} - C_{L_i}^0 \times P_{L_i}(\alpha, \beta|L_i))^2}{\sigma_{L_i}^2} \\ + \sum_{i=1,2,3} \frac{(C_{M_i} - C_{M_i}^0 \times P_{M_i}(\alpha, \beta|M_i))^2}{\sigma_{M_i}^2} \\ + \sum_{i=1,2,3} \frac{(C_{H_i} - C_{H_i}^0 \times P_{H_i}(\alpha, \beta|H_i))^2}{\sigma_{H_i}^2}, \quad (3)$$

where L_i , M_i and H_i represent LE, ME, HE detector groups with the i th FOV, respectively.

The nine FOVs of Insight-HXMT are central-symmetric as shown in Figure 1, and the PSFs of Insight-HXMT are also central-symmetric functions. For a source in the FOV center (on-axis), there is always only one local optimal solution with irregularly shaped confidence contours. For a source deviating from the FOV center (off-axis), there are always two central-symmetric local optimal solutions due to the symmetry of the PSF. With the position information of known sources, one solution can be judged as true and another false. The example and discussion will be presented in Sections 4 and 5.

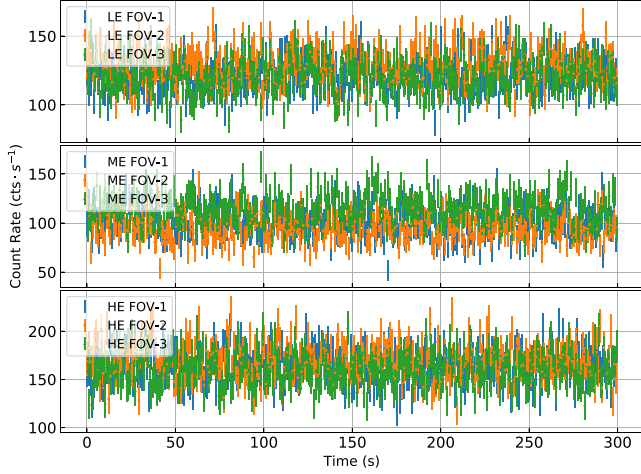


Figure 2. Examples of the Crab light curves (background subtracted) in a pointing observation (ObsID: P0101299008) of Insight-HXMT.

3. Localization with Pointing Observation of the Crab

3.1. Observation and Data

Because the Crab has a stable and high count rate in the three energy ranges of Insight-HXMT, we use the data of all the three telescopes from the Crab to investigate the location capability of Insight-HXMT in pointing observations. Although the Crab Nebular extends to $\sim 2'$ at 1 keV, it still can be considered as a point source for Insight-HXMT observations (Nang et al. 2020). In this paper, we use the Crab observations performed in 2017 August–2019 March (ObsID: P0101299) to test the method.

The data reduction is performed with Insight-HXMT data analysis software package HXMTDAS v2.02 that mainly contains the following steps:

1. Generate calibrated events, with the HXMTDAS tasks of hepical, mepical, megrade (to select events for ME), and lepical, lerecon (to reconstruct events for LE) for HE, ME, and LE instruments, respectively.
2. Good Time Interval selection considering geomagnetic cutoff rigidity ($COR > 10$), elevation angles ($ELV > 10$), the south Atlantic Anomaly and angle distance ($ANG_DIST < 0.05$) with hegtigen, megtigen, megti, and legtigen legti tasks. Event screening to select calibrated events according to GTIs with hescreen, mescreen, and lescreen tasks.
3. Generate light curve from screening files with helcgen, melcgen and lelclgen tasks. Generate light curve background with hebkgmap, mebkgmap and lebkgmap tasks based on the background models of Insight-HXMT (Guo et al. 2020; Liao et al. 2020a, 2020b). The energy ranges used in this paper are 2–6 keV, 7–40 keV, 25–100 keV for LE, ME, HE, respectively.

Examples of the Crab light curves used in this paper are shown in Figure 2.

3.2. Accuracy of Localization

In order to estimate the location accuracy of the pointing observation of Insight-HXMT with different exposures (T_{exp}), the data of the Crab are divided into 11 groups with T_{exp} increasing exponentially from 1 to 1024 s. The statistical error, systematic error, mean deviation are calculated for each exposure. The systematic errors are the intrinsic dispersion of measuring result that can be calculated by solving the equation as:

$$\sum_i \frac{(f_i - \bar{f})^2}{\sigma_{t,i}^2} = N - 1, \quad (4)$$

where

$$\sigma_{t,i}^2 = \sigma_{\text{sys}}^2 + \sigma_{\text{stat},i}^2, \quad (5)$$

$$\bar{f} = \sum_i f_i \times w_i, \quad w_i = \frac{\frac{1}{\sigma_{t,i}^2}}{\sum_i \frac{1}{\sigma_{t,i}^2}}, \quad (6)$$

and σ_{sys} is the systematic error, f_i and $\sigma_{\text{stat},i}$ the measured positions and their statistic errors, and $\sigma_{t,i}$ the total errors. $\sigma_{\text{stat},i}$ are generated in the data fitting process, and can be roughly equivalent to the transmitted statistical errors of the fitted data. The process of error transmission depends on the fitting model as described in Equations (1)–(3).

Figure 3 shows the fitting positions with $T_{\text{exp}} = 1024$ s. The mean deviation from the fitting positions to the actual position of the Crab is about $0^{\circ}009$. Figure 4 shows the statistical and systematic errors of localization in different exposures. The statistical error decreases from $0^{\circ}23$ to $0^{\circ}005$ as the exposure increases from 1 s to 1024 s, and the systematic error is dominant for $T_{\text{exp}} > 128$ s. For the exposure of 1024 s, the systematic error is $0^{\circ}014$, and the total error is $0^{\circ}015$. The systematic error is mainly contributed by the uncertainties of the PSF model and the background estimates. The dependence of the uncertainty of the PSF model on the exposure is weak. However, the uncertainty of background estimates is anti-correlated with the exposure according to the method for background estimates of Insight-HXMT (Guo et al. 2020; Liao et al. 2020a, 2020b). Thus, a trend of the systematic error decreasing with exposure is presented (Figure 4). The quantitative calculations indicate that the uncertainty of background estimates dominates the systematic error for $T_{\text{exp}} < 32$ s, and the uncertainty of the PSF model become the primary contributor for $T_{\text{exp}} > 32$ s. For example, the uncertainties of background estimates for LE, ME and HE are $\sim 4\%$ with $T_{\text{exp}} = 1024$ s, thus the systematic error of localization caused by the uncertainty of background estimates

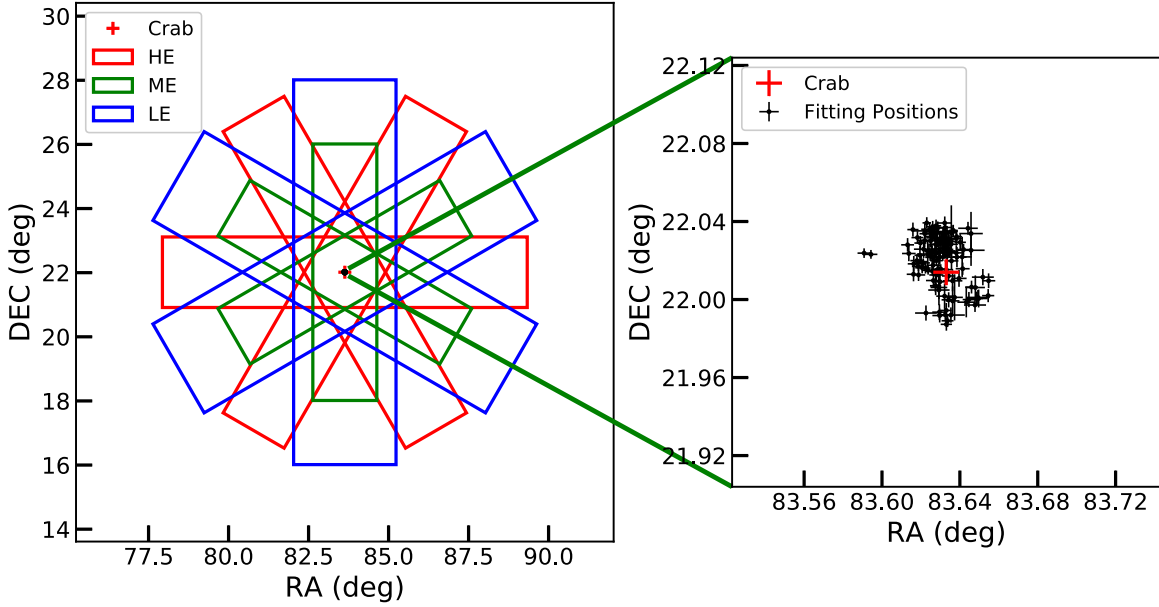


Figure 3. The fitting Crab positions obtained from 25 pointing observations with $T_{\text{exp}} = 1024$ s. The mean deviation from fitting positions to the actual position of the Crab is about $0^{\circ}009$.

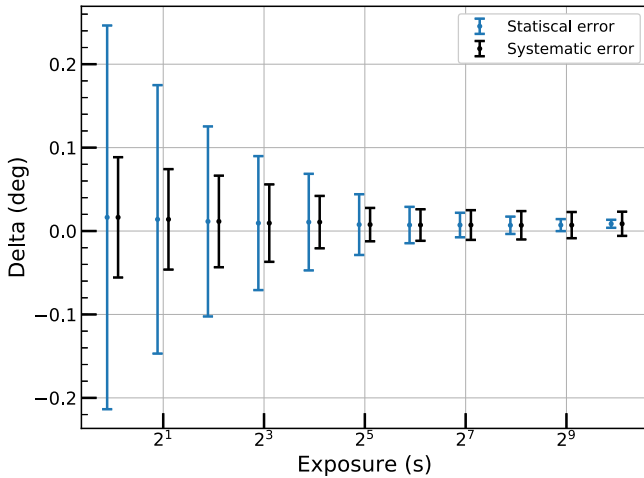


Figure 4. The localization deviation and error of the Crab pointing observations with different exposures. The points are the mean deviations from the fitting positions to the actual position. The blue and black error bars are statistical and systematic errors, respectively.

is evaluated as $\sim 0^{\circ}002$ that is negligible compared to that caused by the PSF model.

4. Application in the Observation of Insight-HXMT

4.1. Distinguishing X-Ray Bursts from GX 354-0 and H 1730-333

GX 354-0 and H 1730-333 are two X-ray sources with an angular distance $\sim 0^{\circ}5$. The two sources were covered

simultaneously by Insight-HXMT in a pointing observation (ObsID: P0214064), in which H 1730-333 is in the FOV center (on-axis) and GX 354-0 is $0^{\circ}5$ from the FOV center (off-axis). As the count rates of GX 354-0 and H 1730-333 in HE are too low to be distinguished from backgrounds, we only use LE and ME data of GX 354-0 and H 1730-333. The upper panel of Figure 5 shows a part of the count rate curve of the pointing observation (ObsID: P0214064), where dozens of X-ray bursts were detected. All the bursts can be roughly divided into two types according to the ratio of the count rate in different FOVs. The details of the two types of bursts are shown in the lower two panels, respectively. For Type A burst, the count rates in all FOVs are nearly consistent with each other both for LE and ME. However, the count rates in FOV-3 are higher than those in FOV-1 for a Type B burst.

The difference in count rates of different FOVs indicates that the two types of X-ray bursts may come from different directions. Figure 6 shows the positions fitted with all the bursts in the light curve of the pointing observation (ObsID: P0214064). Most of the bursts (black points) are contributed by H 1730-333, since their positions near the FOV center are close to the actual position of H 1730-333, with a mean deviation of $0^{\circ}132$ (refers to the mean deviation of each point, and the deviation of the mean position is $0^{\circ}043$). For the off-axis sources, this localization method gives two central-symmetric local optimal solutions due to the symmetry of the PSFs. With the position information of the known sources (e.g., SIMBAD), we can determine that the burst (blue point) belongs

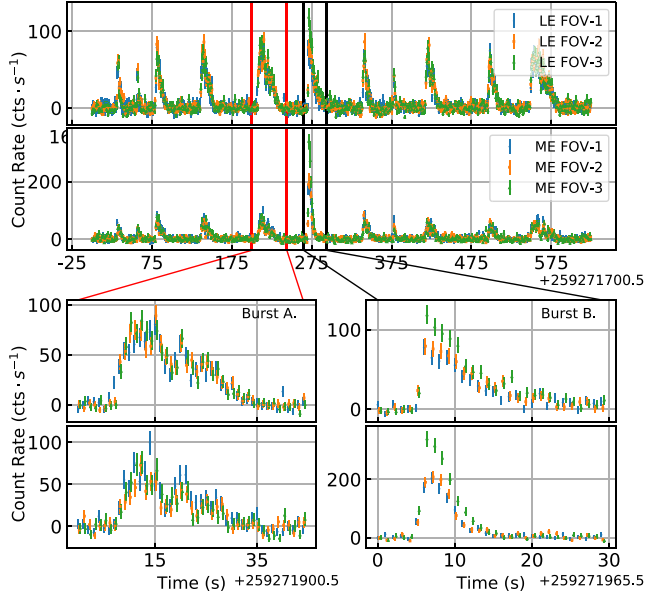


Figure 5. The light curve of an Insight-HXMT pointing observation (ObsID: P0214064003) that some of the bursts are contributed by H 1730–333, which is located in the FOV center, and one belongs to GX 354–0, which is located in the FOV but off-center by $\sim 0.5^\circ$. According to the ratio of the count rate in different FOVs, all the bursts can be roughly divided into two types according to the ratio of the count rate in different FOVs. The details of the two types of bursts are shown in the lower two panels, respectively.

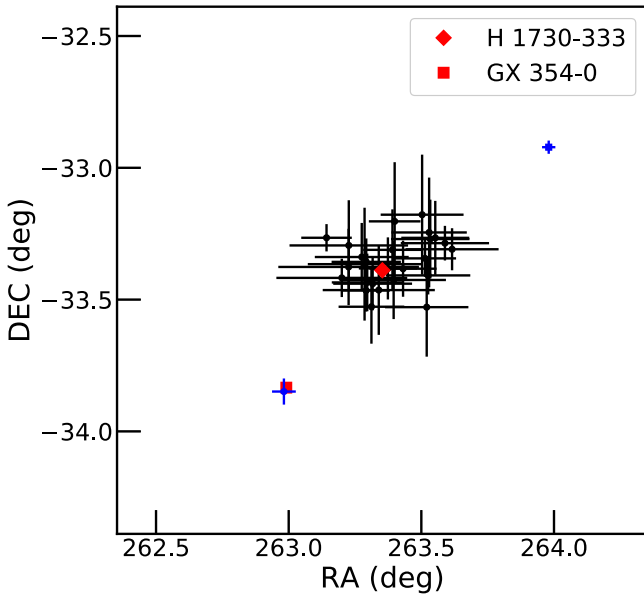


Figure 6. The fitting positions of all the bursts in the light curve of the pointing observation to H 1730–333. This result indicates that most of the bursts (black points) are contributed by H 1730–333 with a mean deviation of 0.132° , and only one burst is contributed by GX 354–0 (blue point) with the deviation of 0.016° .

to GX 354–0 with the deviation of 0.016° , which will be discussed in Section 5.

4.2. Locating the X-Ray Burst from SGR J1935+2154

On 2020 April 28, Insight-HXMT was conducting a long target-of-opportunity observation on the active magnetar SGR J1935+2154. A pair of FRB-like bursts (termed FRB 200428) separated by 29 ms were captured by the Canadian Hydrogen Intensity Mapping Experiment (CHIME) radio telescope (CHIME/FRB Collaboration et al. 2020) and the Survey for Transient Astronomical Radio Emission 2 (STARE2) (Bochenek et al. 2020). All three telescopes of Insight-HXMT detected the X-ray burst from the magnetar 8.62 s before the FRB reached the Earth. The time delay of 8.62 s is exactly the calculated dispersion delay (8.62 s) between X-ray and radio using the dispersion measure (about 333 pc cm^{-3}) determined by CHIME/FRB and STARE2 (Li et al. 2021). This X-ray burst has an extremely high flux. According to the pointing observation localization method, we used the data of the three telescopes of Insight-HXMT to jointly locate the X-ray bursts from the direction of SGR J1935+2154.

For FRB 200428, the large FOV radio telescopes have relatively large positional errors, e.g., the error of STARE2 is several degrees (Bochenek et al. 2020) and the systematic error of CHIME is 1° (the statistical error is subdominant) (CHIME/FRB Collaboration et al. 2020), thus they cannot independently conclude that the FRB came from the magnetar SGR J1935+2154. However, the pointing observation localization method of Insight-HXMT accurately located the high-energy counterpart burst (Li et al. 2021). The difference between the best fitting position of the X-ray bursts and the position of SGR J1935+2154 is $3/7$ with 1σ uncertainty of $10'$, which is completely consistent with SGR J1935+2154 (Li et al. 2021). INTEGRAL also located the X-ray burst, with a 90% confidence interval error of $1/4$, which differs by 0.5 from SGR 1935+2154 (Mereghetti et al. 2020). It is thus confirmed that the X-ray burst came from the magnetar SGR J1935+2154.

5. Discussion and Summary

We have developed a method to locate X-ray sources with pointing observations of Insight-HXMT, and then the pointing observations of the Crab with different exposures are used to investigate the capabilities of this method. With increasing exposures (1 s to 1024 s), the statistical error of localization decreases from 0.23° to 0.005° . All the uncertainties, which can result in the fitting deviation of the detector groups with each FOV, will bring the systematic error of localization. The systematic error caused by response matrix is very small. The uncertainty of the energy-channel relationship, which can lead

to the uncertainty of the observed count rate of a fixed energy range, is negligible. The systematic error mainly originates from the uncertainties of the PSF model and background estimation, and the proportion of the two components depends on the exposure. For the exposure <32 s, the largest proportion of the systematic error is contributed by the uncertainty of background estimates; while for the exposure >32 s, the uncertainty of the PSF model becomes the primary contributor. With the exposure of 1024 s, the systematic error is dominated by the uncertainty of the PSF model and the value $0^{\circ}.014$ is comparable with that of the scanning observation (Nang et al. 2020). It is worth noting that the empirical expression for PSF is approximately centrosymmetric (Section 2), which can lead to two solutions that are symmetrical to each other relative to the FOV center. When the source is relatively strong or far away from the FOV center, the two symmetric local optimums are clearly distinguished. In this case, one solution will be very close to the position of a source in the known sources catalog and will be judged to be true (e.g., GX 354–0 in Section 4.1); while the other solution will be ignored because no corresponding known source can be found. When the source is too weak and closer to the FOV center, the 1-sigma confidence interval will contain both the two symmetric solutions. The localization result in this case is usually near the FOV center but with a large error (SGR J1935+2154 in Section 4.2).


In the application of Section 4, GX 354–0 is located in the FOV but off-center by $\sim 0^{\circ}.5$. This method can effectively distinguish the bursts of GX 354–0 and H 1730–333, so as to eliminate the pollution source in the data analysis of Insight-HXMT (Chen et al. 2021). For a usual pointing observation, there is only one target in the FOV to ensure the accuracy of the scientific result. However, due to the relatively large FOV, the possibility that other source will change from quiescent to active state in the FOV cannot be ignored in future pointing observation. For this more general case, the method can still be applied to distinguish these sources in the FOV. The pointing observation localization method of Insight-HXMT is applied to locate the high-energy counterpart of FRB 200428, and participated in the first discovery that FRB originates from magnetar. It gives an accurate location of the X-ray bursts 3/7 from SGR J1935+2154, within a 1σ uncertainty of $10'$ (Li et al. 2021). We expect that the pointing observation localization method can play a unique role in studying more astronomical events. In the future, the PSF will be more accurate with the accumulation of calibration data and the location accuracy of this method will also be improved.

Acknowledgments

This work made use of the data from Insight-HXMT mission, a project funded by China National Space Administration (CNSA) and the Chinese Academy of Sciences (CAS). The authors thank supports from the National Key R&D Program of China (2021YFA0718500), the National Natural Science Foundation of China under Grant Nos. U1838202, U1838201, U2038102, and U1838113, and the Youth Innovation Promotion Association of the CAS (Grant No. 2018014). This work was partially supported by International Partnership Program of Chinese Academy of Sciences (Grant No. 113111KYSB20190020).

ORCID iDs

Qi Luo  <https://orcid.org/0000-0003-1853-7810>

Jin-Yuan Liao  <https://orcid.org/0000-0001-8277-6133>

References

- Barthelmy, S. D., Barbier, L. M., Cummings, J. R., et al. 2005, *SSRv*, **120**, 143
 Bochenek, C. D., Ravi, V., Belov, K. V., et al. 2020, *Natur*, **587**, 59
 CHIME/FRB Collaboration, Andersen, B. C., Bandura, K. M., et al. 2020, *Natur*, **587**, 54
 Cao, X., Jiang, W., Meng, B., et al. 2020, *SCPMA*, **63**, 249504
 Chen, Y., Cui, W., Li, W., et al. 2020, *SCPMA*, **63**, 249505
 Chen, Y. P., Zhang, S., Zhang, S. N., et al. 2021, *ApJ*, **913**, 150
 Guan, J., Lu, F.-J., Zhang, S., et al. 2020, *JHEAp*, **26**, 11
 Guo, C.-C., Liao, J.-Y., Zhang, S., et al. 2020, *JHEAp*, **27**, 44
 Harrison, F. A., Craig, W. W., Christensen, F. E., et al. 2013, *ApJ*, **770**, 103
 Hiroi, K., Ueda, Y., Hayashida, M., et al. 2013, *ApJS*, **207**, 36
 Israel, G. L., Rea, N., Coti Zelati, F., et al. 2014, *ATel*, **6370**, 1
 Jansen, F., Lumb, D., Altieri, B., et al. 2001, *A&A*, **365**, L1
 Li, C. K., Lin, L., Xiong, S. L., et al. 2021, *NatAs*, **5**, 378
 Li, T.-P., & Wu, M. 1993, *Ap&SS*, **206**, 91
 Li, T.-P., & Wu, M. 1994, *Ap&SS*, **215**, 213
 Li, X., Li, X., Tan, Y., et al. 2020, *JHEAp*, **27**, 64
 Liao, J.-Y., Zhang, S., Chen, Y., et al. 2020b, *JHEAp*, **27**, 24
 Liao, J.-Y., Zhang, S., Lu, X.-F., et al. 2020a, *JHEAp*, **27**, 14
 Liu, C., Zhang, Y., Li, X., et al. 2020, *SCPMA*, **63**, 249503
 Lorimer, D. R., Bailes, M., McLaughlin, M. A., Narkevic, D. J., & Crawford, F. 2007, *Sci*, **318**, 777
 Margalit, B., Beniamini, P., Sridhar, N., & Metzger, B. D. 2020, *ApJL*, **899**, L27
 Matsuoka, M., Kawasaki, K., Ueno, S., et al. 2009, *PASJ*, **61**, 999
 Mereghetti, S., Savchenko, V., Ferrigno, C., et al. 2020, *ApJL*, **898**, L29
 Nang, Y., Liao, J.-Y., Sai, N., et al. 2020, *JHEAp*, **25**, 39
 Petroff, E., Hessels, J. W. T., & Lorimer, D. R. 2019, *A&ARv*, **27**, 4
 Predehl, P., Andritschke, R., Böhringer, H., et al. 2010, *Proc. SPIE*, **7732**, 77320U
 Ridnaia, A., Svinkin, D., Frederiks, D., et al. 2021, *NatAs*, **5**, 372
 Sai, N., Liao, J.-Y., Li, C.-K., et al. 2020, *JHEAp*, **26**, 1
 Stamatikos, M., Malesani, D., Page, K. L., & Sakamoto, T. 2014, *GCN*, **16520**, 1
 Tavani, M., Casentini, C., Ursi, A., et al. 2021, *NatAs*, **5**, 401
 Ubertini, P., Lebrun, F., Di Cocco, G., et al. 2003, *A&A*, **411**, L131
 Weisskopf, M. C., Brinkman, B., Canizares, C., et al. 2002, *PASP*, **114**, 1
 Zhang, S.-N., Li, T., Lu, F., et al. 2020, *SCPMA*, **63**, 249502